

A control-oriented modular one-dimensional model for wall-flow diesel particulate filters

Journal Title
XX(X):1–20
©The Author(s) 2016
Reprints and permission:
sagepub.co.uk/journalsPermissions.nav
DOI: 10.1177/ToBeAssigned
www.sagepub.com/


Soroosh Hassanpour¹ and John McPhee¹

Abstract

A comprehensive modular one-dimensional physics-based mathematical model is developed for non-isothermal compressible flow, pressure drop, and filtration and regeneration processes in wall-flow diesel particulate filters. Employing a modified orthogonal collocation method and symbolic computation in Maple™, the governing partial differential equations are reduced to a control-oriented model governed by ordinary differential equations which can be solved in real time. Numerical examples are provided to indicate the accuracy and computational efficiency of the developed model and to study the different behaviors of wall-flow diesel particulate filters.

Keywords

Diesel particulate filter, compressible flow, filtration, pressure drop, regeneration, model order reduction, control-oriented modeling, orthogonal collocation method

Introduction

Due to a better efficiency compared to spark-ignited engines (*e.g.* gasoline engines), diesel engines (also known as compression-ignition engines) are steadily increasing their market share in many countries. New diesel engines, however, have to comply with continuously tightening legislation on particulate matter (soot or black carbon) and NO_x emissions. Diesel particulate matter cannot be removed or converted into less hazardous compounds by using a traditional catalytic converter¹. In this regard, the idea of a diesel particulate filter (DPF), consisting of either a fibrous or a porous ceramic medium to remove diesel particulate matter (ash and soot) from the exhaust gas of a diesel engine, has received much attention². The most popular DPFs are cellular (honeycomb) ceramic (cordierite, silicon carbide, or aluminum titanate) wall-flow filters which can capture more than 85% of the harmful diesel particulate matter. However, the wall-flow DPFs produce a (non-negligible) back-pressure and require regular maintenance to remove the accumulated soot and ash. Soot is normally removed from the DPF through a regular on-board passive or active process known as filter regeneration in which soot is burned off and ash is left behind. Ash, by definition, is incombustible and should be removed from the DPF through a much less regular cleaning process, *e.g.* by utilizing reverse flow of air through the DPF to blow out the accumulated material³.

With increasing demands for wall-flow DPFs⁴, modeling of their behavior under different operating conditions has become more important. Fast (or even real-time) computer models are required for design and optimization of DPFs as well as controlling the engine combustion, devising and controlling efficient regeneration schemes, deciding about the intervals between the regeneration cycles, and on-board diagnostics of DPFs^{5–7}. In model development, a critical challenge is including the significant features of the DPF while keeping the model order as low as possible.

A number of lumped, one-dimensional (1D), and two-dimensional (2D) models for regeneration, filtration, and pressure drop of DPFs have been presented and verified, through experiments or by comparison against three-dimensional (3D) computational fluid dynamics (CFD) models. Extensive mathematical models have been developed to describe the (catalytic and non-catalytic) thermal regeneration of DPFs. Bissett and Shadman^{2:8:9} developed mathematical models for thermal regeneration of wall-flow DPFs.

¹Systems Design Engineering, University of Waterloo, ON, Canada

Corresponding author:

Soroosh Hassanpour, Systems Design Engineering, University of Waterloo, 200 University Avenue West, Waterloo, Ontario, Canada N2L 3G1.

Email: soroosh@uwaterloo.ca

Koltsakis and Stamatelos^{10–12} extended the models of Bissett and Shadman to account for incomplete soot oxidation and catalytic regeneration effects. A few other lumped and 2D thermal regeneration models were also developed^{7,13}, but have received less attention compared to the models developed by Bissett and Shadman. Indeed, the 1D thermal regeneration model of Bissett⁹ (and its extension by Koltsakis and Stamatelos¹²) is probably the most well-received mathematical tool for representing the non-isothermal compressible flow and heat transfer in DPF channels during regeneration. There is not, however, a widely-accepted mathematical model for the filtration and pressure drop of wall-flow DPFs. Instead there are many different lumped, 1D, and 2D models^{5–7,13–23} and none of these appear to be promising as a general tool applicable to different DPF designs and operating conditions. Hereof, the 1D across-the-wall models developed by Haralampous *et al.*⁶, Torregrosa *et al.*²⁴, and Serrano *et al.*²⁵ seem to be the most comprehensive models available in the literature.

Many of the aforementioned regeneration, filtration, and pressure drop models do not take into account the transient terms of the flow and the effect of exhaust gas pressure on its density. Instead, these models are based on considering a quasi-steady-state compressible flow where the gas density is only related to the gas temperature and the (constant) ambient pressure. Therefore, they are inappropriate for modeling DPFs subject to transient flows (*e.g.* DPFs placed upstream of the turbocharger and those used in off-road applications) or highly loaded DPFs where the pressure drop is high enough to necessitate considering pressure variation effects on the exhaust gas density. There are only a few models in which an unsteady and fully compressible flow is considered inside the channels of wall-flow DPFs^{24–28}. Except for the model developed by Piscaglia and Ferrari²⁸, these models lack a 1D regeneration formulation (*i.e.* they use lumped equations to calculate the deposit layer thickness which is assumed to be constant along the inlet channel length). Apart from Torregrosa *et al.*²⁴ and Serrano *et al.*²⁵, previous models also lack 1D across-the-wall filtration and pressure drop formulations (*i.e.* they assume small deposit and substrate layer thicknesses and use average in-wall variables in their formulations). In addition, a difficulty with most of the aforementioned filtration and pressure drop models is that they are incapable of representing the nonlinear pressure drop behavior of DPFs during transient loading, when the deep bed filtration is transforming into the surface filtration²⁰. The filtration and pressure drop model developed by Serrano *et al.*²⁵ is one of the few available models that can capture this nonlinear pressure drop

behavior. Finally, all of the available 1D models are set up as numerical models (based on computational finite difference and finite element approaches) with high computational costs, which makes them unsuitable for model-based design, optimization, and control developments. In summary, there is no comprehensive 1D DPF model in the literature that:

- represents all features of the DPF operation (*i.e.* its nonlinear pressure drop, filtration, and regeneration) by using 1D equations,
- considers transient and fully compressible non-isothermal flow inside DPF channels,
- and, at the same time, is applicable for model-based control development and computationally inexpensive to solve.

The first goal of the present study is to develop a comprehensive modular physics-based mathematical model for regeneration, filtration, and pressure drop of wall-flow monolithic DPFs that is capable of:

- representing the full transient behavior of the non-isothermal compressible flow inside the channels,
- taking into account the couplings between the pressure variation and thermal effects (during filtration and regeneration) and the compressible gas flow inside the channels,
- and illustrating the nonlinear pressure drop behavior which is known to take place during the transition from deep-bed filtration to surface filtration.

The second goal of this study is to address and implement a method to symbolically convert the developed 1D model (governed by partial differential equations) into a control-oriented model (governed by a set of ordinary differential equations) that can be simulated in real time and be used for model-based control development.

These goals are pursued in the following sections to develop the desired control-oriented 1D DPF model. The developed model is validated by comparing its results against theoretical and experimental results available in the literature. Numerical results are also used to illustrate the appropriateness of the model for real-time applications.

Physics-Based Mathematical Model

Ceramic wall-flow monoliths, shown in Figure 1, are derived from the flow-through cellular substrates (*i.e.* extruded porous ceramic materials) by plugging the opposite ends of adjacent channels in a checkerboard pattern. They consist of many parallel channels, typically of square cross-section,

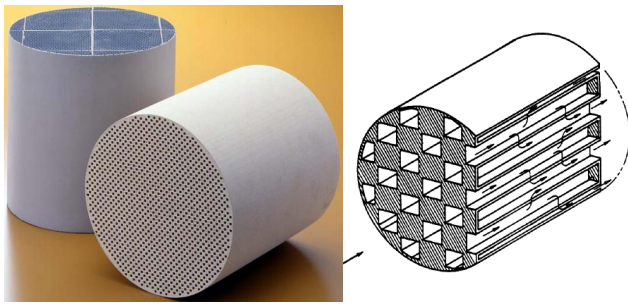


Figure 1. Wall-flow monolithic diesel particulate filters; left: actual silicon carbide and cordierite filters²⁹ (courtesy of NGK), right: schematics of channels and flow⁹.

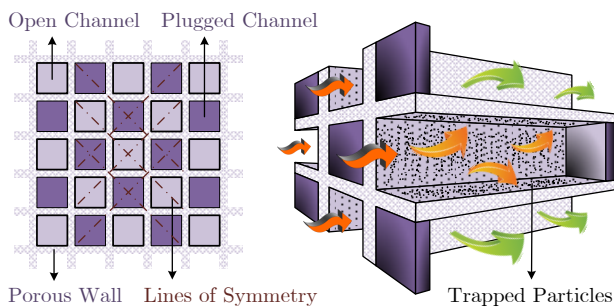


Figure 2. Schematics of channels and flow pattern in a wall-flow monolithic diesel particulate filter.

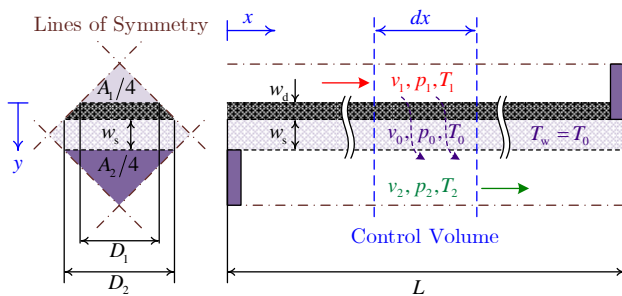


Figure 3. Schematic geometry of a quarter inlet/outlet channel set, considered control volume, and flow pattern.

running axially through the DPF and are distinguished by their high surface area per unit volume and filtration efficiency. As shown in Figure 2, the plugged ends of the upstream (inlet) channels force the diesel exhaust carrying the soot particles to flow through the porous substrate which act as a mechanical filter. The porosity of the substrate is chosen to trap the soot particles at the lateral surfaces of the inlet channels. The first trapped particles form a layer (cake) of deposit which will help in filtering the subsequent soot particles.

The purpose of this section is to develop a modular comprehensive 1D model for a ceramic wall-flow monolithic filter. The model should account for both filtration and

regeneration processes and includes sub-model modules for the fluid dynamics of the exhaust gas inside the filter channels, the filtration process and its associated pressure drop across the porous walls, the convective heat exchanges between the exhaust gas and the channel walls and the axial heat conduction in the channel walls, and the reaction kinetics of the soot oxidation. The equations representing these sub-models will be solved along with the exhaust gas state and property equations, as a separate sub-model module, and the proper initial and boundary conditions, which can also be considered as a module of the model. These are explained in more detail in the following subsections. Note that in this paper the word “wall” is used to collectively represent both the porous ceramic substrate of the filter and the porous deposit layer formed by the accumulated particles.

Assumptions

The main assumption, necessary for a 1D model development, is that all the inlet channels have the same geometry, flow, filtration, thermal, heat transfer, and chemical characteristics, as do the outlet channels. This assumption is supported by the flow self-adjustment resulting in an identical deposit layer across the inlet channels^{9;17}. The pressures, velocities, temperatures, and deposit layer thickness are averaged values over the channel cross-sectional area or the wall thickness and only vary in the axial direction. Most notably, the wall-flow temperature and the wall (filter substrate plus deposit layer) temperature are considered to be equal and constant over the wall thickness and the wall-flow pressure is assumed to be the mean value of the pressures in the inlet and outlet channels and constant over the wall thickness. The other model assumptions used in this study are stated in the following subsections.

Considering these assumptions and the schematics and the lines of symmetry shown in Figure 2, it is sufficient for modeling purposes to only consider a quarter inlet/outlet channel set. As shown in Figure 3, this set includes one quarter of an inlet channel and one quarter of an adjacent outlet channel.

A differential control volume in the axial direction (x -axis), as shown in Figure 3, is used to derive the required governing equations. The independent variables are time (t) and axial coordinate (x) and the main dependent variables are velocity (v), pressure (p), and temperature (T) in the representative inlet and outlet channels and in the wall (respectively denoted by $v_1, p_1, T_1, v_2, p_2, T_2$, and v_0, p_0, T_0) along with the deposit layer thickness (w_d). Recall that the local wall temperature T_w is assumed to be equal to the

local wall-flow temperature T_0 (*i.e.* $T_w = T_0$) and, therefore, is not a separate variable.

Geometry

The changes in the geometry of the channels due to the thermal effects (*e.g.* thermal expansions) are assumed to be negligible. Moreover, the thickness of the plugging sections at the opposite ends of the inlet and outlet channels is considered to be negligible compared to the length of the channels. Therefore, the inlet and outlet channels have the same constant length L . Due to the filtration and regeneration processes (*i.e.* accumulation and oxidation of particles), however, the inlet and outlet channels have different widths D_1 (which is time-varying) and D_2 (which is constant). Based on Figure 3, one can write:

$$D_1 = D_2 - 2w_d = D_2 \left(1 - \frac{2w_d}{D_2}\right), \quad (1)$$

where w_d is the deposit layer thickness (which varies with time during the filtration and regeneration processes). Then, the cross-sectional perimeters P_i and areas A_i of the inlet and outlet channels, corresponding to the quarter inlet/outlet channel set shown in Figure 3, will be:

$$\begin{aligned} \frac{P_1}{4} = D_1, & \quad \frac{A_1}{4} = \frac{D_1^2}{4}, \\ \frac{P_2}{4} = D_2, & \quad \frac{A_2}{4} = \frac{D_2^2}{4}. \end{aligned} \quad (2)$$

In addition, the cross-sectional areas of the filter substrate and the deposit layer corresponding to the quarter inlet/outlet channel set shown in Figure 3 may be obtained as:

$$\begin{aligned} \frac{A_s}{4} &= \left(D_2 + \frac{w_s}{2}\right) w_s = D_2 w_s \left(1 + \frac{w_s}{2D_2}\right), \\ \frac{A_d}{4} &= \left(D_2 - w_d\right) w_d = D_2 w_d \left(1 - \frac{w_d}{D_2}\right), \end{aligned} \quad (3)$$

where w_s is the thickness of the porous ceramic substrate (which is a constant).

Fluid Dynamics

Fully-developed flows with negligible gravity and vehicle acceleration effects are considered inside the channels. The changes in the mass flow rate due to the filtration or regeneration are taken to be insignificant. In addition, the quasi-steady wall-flow is assumed to be perpendicular to the wall, both when entering the wall and when leaving it, with properties that are averaged over the wall thickness. Considering these assumptions and the control volume shown in Figure 3 and using the general 1D Reynolds

transport theorem³⁰, one can derive the conservation of mass, linear momentum, and energy equations for the inlet and outlet channels of the DPF.

The continuity (conservation of mass) equation for the inlet and outlet channels may be written as:

$$\frac{\partial}{\partial t} (\rho_i A_i) + \frac{\partial}{\partial x} (\rho_i A_i v_i) - (-1)^i (\rho_0 P_2 v_0) = 0, \quad (4)$$

where equations (1) and (2) are recalled and $i = 1$ corresponds to the inlet channel and $i = 2$ indicates the outlet channel. In equation (4), ρ_i and v_i ($i = 1, 2$) represent the density and velocity of the exhaust gas inside the inlet and outlet channels and ρ_0 and v_0 are the density and velocity of the exhaust gas inside the porous wall. In equation (4), $\rho_0 P_2 v_0$ represents the average in-wall mass flow rate per unit length of the channel (see the Appendix).

Similarly, the linear momentum equations in the axial direction, *i.e.* x -axis, may be obtained as:

$$\begin{aligned} \frac{\partial}{\partial t} (v_i \rho_i A_i) + \frac{\partial}{\partial x} (\sigma_i \rho_i A_i v_i^2) \\ + A_i f_i \left(\frac{1}{D_i}\right) \left(\frac{1}{2} \rho_i v_i^2\right) + A_i \frac{\partial p_i}{\partial x} = 0, \end{aligned} \quad (5)$$

where p_i represents the pressure of the exhaust gas at the inlet and outlet channels, σ_i is the linear momentum coefficient which can be calculated from the assumed flow profile in the channels³⁰, and f_i is the friction coefficient. In general, the friction coefficient f_i is a function $\phi_{f,i}$ of the channel Reynolds number Re_i and relative roughness $\frac{\epsilon_i}{D_i}$ ³⁰:

$$f_i = \phi_{f,i}(Re_i, \frac{\epsilon_i}{D_i}) = \phi_{f,i}\left(\frac{\rho_i v_i D_i}{\mu_i}, \frac{\epsilon_i}{D_i}\right), \quad (6)$$

where μ_i is the (dynamic) viscosity of the exhaust gas in the inlet and outlet channels. Assuming a fully-developed laminar flow of the exhaust gas inside the square cross-section channels of the DPF, one can simply write³¹:

$$f_i = \phi_{f,i}(Re_i) = \frac{C_{f,i}}{Re_i} = \frac{C_{f,i} \mu_i}{\rho_i v_i D_i}, \quad C_{f,i} = 56.92. \quad (7)$$

Alternatively, one can use the more accurate equation suggested by Bissett *et al.*³²

Analogously, the conservation of energy equations for the inlet and outlet channels will be derived as:

$$\begin{aligned} \frac{\partial}{\partial t} \left(\left(u_i + \sigma_i \frac{v_i^2}{2} \right) \rho_i A_i \right) \\ + \frac{\partial}{\partial x} \left(\left(h_i + \kappa_i \frac{v_i^2}{2} - \frac{4}{3} \frac{\mu_i}{\rho_i} \frac{\partial v_i}{\partial x} \right) \rho_i A_i v_i \right) \\ - (-1)^i \left(\left(h_0 + \frac{v_0^2}{2} \right) \rho_0 P_2 v_0 \right) = \dot{q}_i, \end{aligned} \quad (8)$$

where u_i is the exhaust gas internal energy in the inlet and outlet channels, h_i and h_0 are the exhaust gas enthalpies at the channels and inside the wall, κ_i is the kinetic energy coefficient calculable from the assumed flow profile in the channels³⁰, and \dot{q}_i is the rate of the heat transferred to the fluid in the channels.

The 6 relations of equations (4), (5), and (8) (obtained by substituting $i = 1, 2$) represent the dynamics of the non-isothermal compressible flow in the channels.

Filtration and Pressure Drop Across the Wall

It is assumed that the particles are uniformly distributed between the inlet channels and particle deposition is directly proportional to the wall-flow mass flow rate. Accumulated ash is assumed to be negligible. The parameters, variables, and equations used to characterize the filtration process and its associated pressure drop are not explicitly dependent on the flow pressures and temperatures. The porosity and mean pore size of the filter substrate and porosity of the deposit layer are assumed to remain constant during the filtration and regeneration. It is also worthwhile to note that the pressure drops associated with expansion and contraction of the flow at the inlet and outlet ducts of the whole DPF are not dealt with in this paper (these can be added as lumped parameter equations if desired).

As noted previously, the average exhaust gas pressure across the wall system (useful for calculation of the gas density inside the wall) is taken to be the mean value of the pressures inside the inlet and outlet channels, *i.e.*:

$$p_0 = \frac{1}{2} (p_1 + p_2). \quad (9)$$

About the filtration efficiency, note that as soon as the first particles are collected by the filter substrate, they bridge over (or aggregate) and start forming a layer or cake of deposit which itself acts as a very fine filter. As a consequence, the filtration efficiency increases as particles are being trapped and the deposit layer is being formed¹⁴. The overall filtration efficiency is defined as the ratio of the mass of particles trapped inside the filter to the total mass of the particles entering the filter. This filtration efficiency η is assumed to increase asymptotically (based on a negative exponential function) as the first particles are being collected and reach its maximum as soon as a deposit layer is initialized, *i.e.*:

$$\eta = \eta_{\max} - (\eta_{\max} - \eta_{\min}) \exp\left(-\frac{w_d}{w_{d,\text{ref}}}\right), \quad (10)$$

where η_{\min} is the clean filter efficiency, η_{\max} is the maximum filtration efficiency achieved after initiation of

a deposit layer, and $w_{d,\text{ref}}$ is a reference deposit layer thickness that can be determined experimentally. Note that this phenomenological equation can be replaced with more complex equations, *e.g.* those suggested by Opris and Johnson¹⁴ or those by Serrano *et al.*²⁵, if a more accurate filtration efficiency calculation is desired. Having the filtration efficiency η and the in-wall mass flow rate per unit length of channel $\rho_0 P_2 v_0$, the rate of change of the deposit layer thickness due to the filtration will be obtained as (see the Appendix):

$$\frac{\partial w_{d,f}}{\partial t} = \frac{1}{\rho_d P_1} (\eta X_1 \rho_0 P_2 v_0), \quad (11)$$

where X_1 is the mass fraction of the particulate matter (*i.e.* mass of particles per unit mass of the exhaust gas) in the inlet channel.

For across-the-wall pressure drop calculations, note that the complexity of the flow pattern inside the porous wall does not allow for an analytic expression to be derived. Many authors have used the quasi-empirical Darcy's law and related the pressure drop to the product of exhaust gas viscosity and the wall-flow velocity^{5;13-15;17;20;22}. For higher wall-flow velocities, an inertial term, *i.e.* the product of exhaust gas density and the wall-flow velocity squared, is known to affect the pressure drop calculations. There have been authors who suggested the addition of this inertial term, *i.e.* Forchheimer's extension^{6;7;9;16;18;19;21}. In these correlations, Darcy's permeability and Forchheimer's inertial coefficients are not easy to interpret, and are to be measured experimentally for different filter substrates and deposit layers. Accordingly, it is preferred in this paper to use a quasi-empirical correlation containing easier-to-measure parameters, like porous media properties, and well-known flow parameters/variables for pressure drop calculations across the DPF porous wall. One such correlation is the Ahmed and Sunada equation (with the same basis as Darcy's law with Forchheimer's extension), which may be considered both a phenomenological and a Navier-Stokes type model, combined with the modified Ergun equation, which includes a model of the porous media^{19;33}. By using this equation and by considering the schematic shown in Figure 3, the assumptions noted previously, and the approach taken by Konstandopoulos *et al.*¹⁷, one can obtain the following expression for the pressure drop across the wall system (see the Appendix):

$$\Delta p = p_1 - p_2 = C_{v_0} v_0 + C_{v_0^2} v_0^2, \quad (12)$$

where:

$$\begin{aligned} C_{v_0} &= \left(\alpha_s D_2 \ln\left(\frac{D_2 + w_s}{D_2}\right) + \alpha_d \frac{D_2}{2} \ln\left(\frac{D_2}{D_1}\right) \right) \mu_0, \\ C_{v_0^2} &= \left(\beta_s \frac{D_2 w_s}{D_2 + w_s} + \beta_d \frac{D_2 w_d}{D_1} \right) \rho_0, \end{aligned} \quad (13)$$

and:

$$\begin{aligned} \alpha_s &= \alpha'_s \frac{(1 - \varepsilon_s)^2}{\varepsilon_s^3 d_s^2}, & \beta_s &= \beta'_s \frac{(1 - \varepsilon_s)}{\varepsilon_s^3 d_s}, \\ \alpha_d &= \alpha'_d \frac{(1 - \varepsilon_d)^2}{\varepsilon_d^3 d_d^2}, & \beta_d &= \beta'_d \frac{(1 - \varepsilon_d)}{\varepsilon_d^3 d_d}. \end{aligned} \quad (14)$$

In equations (13) and (14), μ_0 is the exhaust gas viscosity inside the wall, ε_s and d_s are the ceramic substrate porosity and mean pore size, ε_d and d_d are the deposit layer porosity and mean pore size, and α'_d , β'_d , α'_s , and β'_s are the nondimensional constants of the deposit layer and the ceramic substrate to be determined experimentally. One can assume $\alpha'_d = \alpha'_s = 150$ and $\beta'_d = \beta'_s = 1.75$ ³³. The relation given in equation (12) may be solved to obtain the following expression for the wall-flow velocity v_0 :

$$v_0 = \frac{1}{2C_{v_0^2}} \left(\sqrt{C_{v_0^2}^2 + 4C_{v_0^2} \Delta p - C_{v_0}} \right), \quad (15)$$

where a positive pressure drop (*i.e.* $\Delta p > 0$) implies a positive wall-flow velocity (*i.e.* $v_0 > 0$).

Now it is useful to take into account the nonlinear relationship between the pressure drop and the deposit layer thickness for the limiting case where $w_d \rightarrow 0$ ^{9;14;20}. For this purpose, it can be considered that the first particles trapped by the wall place are close to each other and form a porous medium with small pores of sizes comparable to the size of soot particles. The later trapped particles, however, aggregate or bridge over each other and form a porous medium with larger pores of sizes a few times larger than the size of soot particles. This pore size variation results in a faster increase of the pressure drop in the beginning of the deposit layer formation. Therefore, the mean pore size of the deposit layer d_d is assumed to asymptotically grow as the deposit layer thickness w_d is increased, *i.e.*:

$$d_d = d_{d,\max} - \left(d_{d,\max} - d_{d,\min} \right) \exp\left(-\frac{w_d}{w_{d,\text{cr}}}\right), \quad (16)$$

where $d_{d,\min}$ and $d_{d,\max}$ are the minimum and maximum values of the deposit layer pore size and $w_{d,\text{cr}}$ is a critical thickness—all to be determined experimentally. Although the porosity of the deposit layer may also vary as the deposit layer is being formed, due to a general lack of information about this variation, the porosity of the deposit layer is

assumed to have a constant average value during the filtration and regeneration.

The relations given in equations (9) and (15) are required to complement the fluid dynamic equations derived previously and the relation in equation (11) is useful to obtain one of the key state variables, *i.e.* the deposit layer thickness w_d (see equation (32)).

Heat Transfer

The temperatures of the deposit layer and the filter substrate are taken to be equal and constant over the wall thickness and are collectively represented as the wall temperature. The wall-flow temperature (*i.e.* temperature of the exhaust gas passing through the wall) is equal to this local wall temperature and, therefore, is constant over the wall thickness (*i.e.* the inter-phase heat transfer between the wall and the wall-flow is assumed to be so large that solid and fluid temperatures may be taken to be equal). It is also assumed that there is no heat generation (*e.g.* due to soot oxidation and other chemical reactions) inside the inlet and outlet channels. There are only convection heat transfers inside the channels, between the exhaust gas and the wall, and conduction heat transfer inside the wall, in the axial direction. Considering these assumptions and the schematic shown in Figure 3, the corresponding equations for the heat transfer in the inlet and outlet channels of the DPF can be obtained.

The rate of heat transferred to the fluid in the channels (per unit length of the channel), *i.e.* \dot{q}_i in equation (8), can be written as:

$$\begin{aligned} \dot{q}_i &= q_{i,c} + q_{i,g} = c_i P_i \left(T_w - T_i \right) + 0 \\ &= c_i P_i \left(T_w - T_i \right), \end{aligned} \quad (17)$$

where T_w and T_i are the wall temperature and the exhaust gas temperature inside the channels, $q_{i,c}$ is the convection heat transport in the channels, $q_{i,g}$ is the heat generated in the channels (*e.g.* due to any chemical reaction), and c_i is the local convection heat transfer coefficient in the inlet and outlet channels. Recall that, based on the assumptions, $T_w = T_0$ and $q_{i,g} = 0$.

In addition, one can derive the following equation for the conduction heat transport in the axial direction inside the filter wall (*i.e.* the filter substrate plus the deposit layer) and derive:

$$\begin{aligned} &\left(\rho_s A_s C_{p,s} + \rho_d A_d C_{p,d} \right) \frac{\partial T_w}{\partial t} \\ &- \frac{\partial}{\partial x} \left(\left(k_s A_s + k_d A_d \right) \frac{\partial T_w}{\partial x} \right) = \dot{q}_w, \end{aligned} \quad (18)$$

where ρ_s , k_s , $C_{p,s}$ and ρ_d , k_d , $C_{p,d}$ are the density, thermal conductivity, and specific heat of the filter porous substrate and the porous deposit layer respectively and \dot{q}_w is the rate of heat transferred to the wall per unit length of the channel which can be written as:

$$\begin{aligned}\dot{q}_w &= \dot{q}_{w,c} + \dot{q}_{w,g} \\ &= c_1 P_1 (T_1 - T_w) + c_2 P_2 (T_2 - T_w) + \dot{q}_{w,g},\end{aligned}\quad (19)$$

where $\dot{q}_{w,c}$ is the rate of convection heat transport to the wall and $\dot{q}_{w,g}$ is the rate of the heat generated in the wall (e.g. due to a regeneration process), both per unit length of the channel. Assuming that the regeneration process is the only source of the heat generation in the wall, an expression for $\dot{q}_{w,g}$ is given in equation (30).

The relation in equation (17) complements the conservation of energy relations given by equation (8), which along with equation (18) represent the transportation of the heat in the channels and in the filter wall.

It is worth noting that the thermal conductivity and specific heat of the porous ceramic substrate and the porous deposit layer may be calculated based on their porosity, the properties of their solid phases, and the properties of the wall-flow exhaust gas. For the porous ceramic substrate one can derive^{14,34}:

$$k_s = k_0 \left(1 + \frac{3(1 - \varepsilon_s) \left(\frac{k_{ss}}{k_0} - 1 \right)}{3 + \varepsilon_s \left(\frac{k_{ss}}{k_0} - 1 \right)} \right), \quad (20)$$

$$\rho_s C_{p,s} = (1 - \varepsilon_s) \rho_{ss} C_{p,ss} + \varepsilon_s \rho_0 C_{p,e},$$

where ε_s represents the porosity of the substrate, ρ_{ss} , k_{ss} , and $C_{p,ss}$ are the density, thermal conductivity, and specific heat capacity of the solid (nonporous) ceramic and ρ_0 , k_0 , and $C_{p,e}$ are the properties of the wall-flow exhaust gas. Analogously for the porous deposit layer one can write:

$$k_d = k_0 \left(1 + \frac{3(1 - \varepsilon_d) \left(\frac{k_{sd}}{k_0} - 1 \right)}{3 + \varepsilon_d \left(\frac{k_{sd}}{k_0} - 1 \right)} \right), \quad (21)$$

$$\rho_d C_{p,d} = (1 - \varepsilon_d) \rho_{sd} C_{p,sd} + \varepsilon_d \rho_0 C_{p,e},$$

where ε_d represents the porosity of the deposit layer and ρ_{sd} , k_{sd} , and $C_{p,sd}$ are the density, thermal conductivity, and specific heat capacity of the solid particles (mainly carbon particles) forming the deposit layer.

Also note that by neglecting the entrance effects, the local heat transfer coefficients c_i ($i = 1, 2$), associated with the forced convection heat transport by the 1D flow of the exhaust gas inside the inlet and outlet channels, can be determined from the channel Nusselt number Nu_i which

itself can be expressed as a function $\phi_{Nu,i}$ of the channel Reynolds number Re_i and the channel Prandtl number Pr_i ³¹:

$$c_i = \frac{Nu_i k_i}{D_i}, \quad (22)$$

$$Nu_i = \phi_{Nu,i}(Re_i, Pr_i) = \phi_{Nu,i}\left(\frac{\rho_i v_i D_i}{\mu_i}, \frac{C_{p,e} \mu_i}{k_i}\right),$$

where k_i and $C_{p,e}$ are the thermal conductivity and the (constant pressure) specific heat capacity of the exhaust gas in the inlet and outlet channels. For the cases where the Prandtl number Pr_i of the fluid does not vary appreciably (e.g. for air), equation (22) reduces to³¹:

$$c_i = \frac{Nu_i k_i}{D_i}, \quad (23)$$

$$Nu_i = \phi_{Nu,i}(Re_i) = \phi_{Nu,i}\left(\frac{\rho_i v_i D_i}{\mu_i}\right).$$

By assuming a fully-developed laminar flow of the exhaust gas inside the square cross-section channels of the DPF, one can simply derive $Nu_i = 3.61$ ³¹ or:

$$c_i = \frac{3.61 k_i}{D_i}. \quad (24)$$

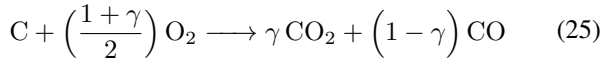
It is also possible to use the more complex and accurate equation suggested by Bissett *et al.*³²

Reaction Kinetics

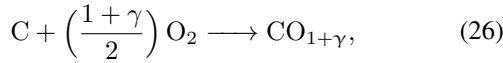
As noted previously, typical diesel particulate matter consists mainly of combustible carbonaceous cores, absorbed compounds, sulfates, and metal oxides which can react with the oxygen present in the exhaust gas. However, the main chemical reaction that is usually considered to occur in a DPF (during the regeneration at sufficiently high temperatures) is the soot particle oxidation, *i.e.* first-order heterogeneous (incomplete) oxidation of carbon. Note that the oxidation of soot particles aided by nitrogen dioxide NO_2 , which is the dominant regeneration mechanism in most catalytic DPFs, is not considered in this work. It is assumed that this oxidation occurs only inside the deposit layer (the oxidation inside the channels or in the filter substrate wall are negligible) and results in shrinkage of the deposit layer without changing its physical properties such as bulk density and porosity. Also, it is assumed that the convection transports of oxygen in the channels and wall dominate the diffusion transports, and that the depletion of oxygen in the reactive deposit layer does not influence the upstream oxygen concentration. Therefore, the oxygen concentration in the inlet channel is assumed to remain constant in the axial

direction, and be equal to the oxygen concentration of the exhaust gas entering the filter.

Usually the soot particle oxidation is represented as the complete oxidation of carbon to carbon dioxide CO_2 ⁹. However, carbon monoxide CO has been observed in noticeable quantities in the reaction products downstream the DPF in several works³⁵, suggesting the possibility of an incomplete oxidation. Based on the relatively large difference between the formation enthalpies of CO and CO_2 , it is expected that an incomplete oxidation significantly affects the heat released during the regeneration and, consequently, the entire regeneration process. In this work, the soot particle oxidation is mathematically modeled as an incomplete carbon oxidation (in the absence of a catalyst). The very complex incomplete carbon oxidation is lumped in (or simplified to) an apparent one-step kinetic scheme based on the following reaction^{10;12}:



or equivalently:



where γ ($0 \leq \gamma \leq 1$) is the index of the completeness of the carbon oxidation.

Considering the aforementioned assumptions and the reaction given by equation (25) or (26), the variation of the oxygen molar concentration across the wall may be derived as (see the Appendix):

$$\begin{aligned} \frac{\Delta Y}{Y_1} &= \frac{Y_1 - Y_2}{Y_1} \\ &= 1 - \exp\left(-S_d K_d \left(\frac{1+\gamma}{2}\right) \frac{w_d}{v_0} \left(1 - \frac{w_d}{D_2}\right)\right), \end{aligned} \quad (27)$$

where Y_1 and Y_2 are the oxygen molar concentrations in the inlet and outlet channels, S_d is the specific surface (or area) of the porous deposit layer, and K_d is the reaction rate coefficient inside the deposit layer which can be expressed as^{2;9;10;12}:

$$K_d = \mathcal{K} T_w \exp\left(\frac{-E}{R_u T_w}\right), \quad (28)$$

where \mathcal{K} is the collisions frequency factor (or reaction rate constant), E is the activation energy of the carbon oxidation, and R_u is the universal gas constant. Note that the molar rate of oxygen depletion (per unit length of the channel), which is of importance for determination of the rate of particle depletion and also the rate of heat generation inside the wall, may be obtained as $\frac{\rho_0 P_2 v_0}{M_e} \Delta Y$, where M_e is the molecular weight (or molar mass) of the exhaust gas. Also,

using equation (25) or (26), the molar rate of the carbon particle depletion (per unit length of the channel) can be calculated as $\frac{\rho_0 P_2 v_0}{M_e} \Delta Y \frac{2}{1+\gamma}$.

Now the rate of change of the deposit layer thickness due to the regeneration (oxidation), *i.e.* $\frac{\partial w_{d,r}}{\partial t}$, can be related to the molar rate of the carbon particle depletion and one can derive (see the Appendix):

$$\frac{\partial w_{d,r}}{\partial t} = \frac{-1}{\rho_d P_1} \left(M_C \frac{\rho_0 P_2 v_0}{M_e} \Delta Y \frac{2}{1+\gamma} \right), \quad (29)$$

where M_C is the molecular weight of carbon. Additionally, the rate of the heat generation per unit length of the channel, inside the wall (or more accurately inside the deposit layer) and due to the carbon particle oxidation, *i.e.* $\dot{q}_{w,g}$ in equation (19), can be obtained as:

$$\dot{q}_{w,g} = H_{\text{CO}_{1+\gamma}} \frac{\rho_0 P_2 v_0}{M_e} \Delta Y \frac{2}{1+\gamma}, \quad (30)$$

where $H_{\text{CO}_{1+\gamma}}$ is the heat or enthalpy of reaction for the incomplete carbon oxidation noted in equation (25) or (26), which can be calculated as a combination of the specific heats or formation enthalpies of CO_2 and CO , H_{CO_2} and H_{CO} :

$$H_{\text{CO}_{1+\gamma}} = \gamma H_{\text{CO}_2} + (1-\gamma) H_{\text{CO}}. \quad (31)$$

The relations given by equations (30) and (31) are used to complement the through-the-wall heat transfer equation in equations (18) and (19), and the relation given by equation (29) is useful to represent the rate of change of the deposit layer thickness w_d (see equation (32)).

Deposit Layer Thickness

Based on equations (11) and (29), when taking into account both the filtration and the regeneration processes, the following relation can be obtained for the overall rate of change of the deposit layer thickness:

$$\begin{aligned} \frac{\partial w_d}{\partial t} &= \frac{\partial w_{d,f}}{\partial t} + \frac{\partial w_{d,r}}{\partial t} \\ &= \frac{\rho_0 P_2 v_0}{\rho_d P_1} \left(\eta X_1 - \frac{M_C}{M_e} \Delta Y \frac{2}{1+\gamma} \right). \end{aligned} \quad (32)$$

State and Property Equations

The equations derived in the previous subsections, governing the fluid dynamics, heat transfer, reaction kinetics, pressure drop, and filtration process inside the DPF, contain parameters which can depend on others and vary in time. Some of these varying parameters, such as the friction coefficient f_i and convection heat transfer coefficient c_i , were defined right after their usage. The purpose of this

section is to define the variable parameters which are functions of the state variables and were not described previously.

Assuming that the exhaust gas is ideal, the equation of state for the exhaust gas (inside the inlet and outlet channels and the wall) may be written as:

$$\rho_i = \frac{p_i}{R_e T_i}, \quad \rho_0 = \frac{p_0}{R_e T_0}, \quad (33)$$

where R_e is the exhaust gas specific gas constant which may be obtained by dividing the universal gas constant R_u by the molecular weight of the exhaust gas M_e , *i.e.* $R_e = \frac{R_u}{M_e}$. Also, the enthalpy of the exhaust gas (in the channels and the wall) is:

$$h_i = C_{p,e} T_i, \quad h_0 = C_{p,e} T_0, \quad (34)$$

and the internal energy of the exhaust gas (in the channels and the wall) may be expressed as:

$$\begin{aligned} u_i &= h_i - \frac{p_i}{\rho_i} = C_{p,e} T_i - R_e T_i = C_{v,e} T_i, \\ u_0 &= h_0 - \frac{p_0}{\rho_0} = C_{p,e} T_0 - R_e T_0 = C_{v,e} T_0, \end{aligned} \quad (35)$$

where $C_{v,e} = C_{p,e} - R_e$ is the constant volume heat capacity of the exhaust gas.

The viscosity and thermal conductivity of the exhaust gas may be calculated according to⁹:

$$\mu_i = C_\mu \sqrt{T_i}, \quad \mu_0 = C_\mu \sqrt{T_0}, \quad (36)$$

and:

$$k_i = (C_{p,e} + C_k) \mu_i, \quad k_0 = (C_{p,e} + C_k) \mu_0, \quad (37)$$

where C_μ and C_k are constant coefficients which are given in Table 1. In addition, the heat capacity for the solid (nonporous) phases of the deposit layer and the ceramic substrate may be obtained from⁹:

$$\begin{aligned} C_{p,ss} &= C_{C_{p,ss,i}} + C_{C_{p,ss,ii}} T_w + C_{C_{p,ss,iii}} T_w^{-2}, \\ C_{p,sd} &= C_{C_{p,sd,i}} + C_{C_{p,sd,ii}} T_w + C_{C_{p,sd,iii}} T_w^{-2}, \end{aligned} \quad (38)$$

where $C_{C_{p,ss,i}}$, $C_{C_{p,ss,ii}}$, $C_{C_{p,ss,iii}}$ and $C_{C_{p,sd,i}}$, $C_{C_{p,sd,ii}}$, $C_{C_{p,sd,iii}}$ are constant coefficients as given in Table 1.

Boundary and Initial Conditions

The partial differential equations governing the processes inside the DPF require appropriate initial and boundary conditions to be solvable. In regard to the initial conditions (ICs) at time $t = 0$, the DPF starts from a static clean

condition, in equilibrium with the ambient pressure and temperature, in which:

$$\begin{aligned} v_1 &= v_2 = 0, & p_1 &= p_2 = p_a, \\ T_1 &= T_2 = T_0 = T_a, & w_d &= 0, \end{aligned} \quad (39)$$

where T_a is the ambient temperature and p_a is the ambient pressure.

About the boundary conditions (BCs) at the beginning of the inlet channel where $x = 0$, it is assumed that the conditions of the exhaust gas entering the DPF, *i.e.* its velocity $v_{e,in}$ and temperature $T_{e,in}$, are known and one can write⁹:

$$\begin{aligned} v_1 &= v_{e,in}, & T_1 &= T_{e,in}, \\ v_2 &= 0, & \frac{\partial T_w}{\partial x} &= 0. \end{aligned} \quad (40)$$

Note that, to get a smooth solution, the inlet exhaust gas conditions should initially be in accordance with the initial conditions noted in equation (39). Also, by assuming that the pressure of the exhaust gas at the end of the outlet channel, *i.e.* $p_{e,out}$, is known (*e.g.* equal to the ambient pressure), the BCs at the end of the outlet channels where $x = L$ can be written as:

$$\begin{aligned} p_2 &= p_{e,out}, \\ v_1 &= 0, & \frac{\partial T_w}{\partial x} &= 0. \end{aligned} \quad (41)$$

It is worthwhile to note that by substitution from the BCs in equations (40) and (41) into the linear momentum equations given by equation (5) one can derive two extra BCs as:

$$\begin{aligned} \text{at } x = 0 : & \quad \frac{\partial p_2}{\partial x} = 0, \\ \text{at } x = L : & \quad \frac{\partial p_1}{\partial x} = 0, \end{aligned} \quad (42)$$

which may be useful when solving the DPF equations numerically.

Model Order Reduction

As noted previously, the second goal of this study is to convert the comprehensive 1D model of wall-flow DPFs, developed in the previous section as the first goal, into a control-oriented model which is still accurate but can be solved in real-time. Such a computer model will be useful for design optimization and advanced controller development. The equations of the DPF model, derived in the previous section, can be combined into a set of 8 nonlinear partial differential equations (PDEs). However, achieving a real-time simulation of this set of PDEs, where variables change in time and axial direction (*i.e.* x -axis), is a challenge.

There are several approximation schemes by which the spatial domain of the model can be discretized and the governing PDEs can be reduced or converted into a system of ordinary differential equations (ODEs) that can be solved efficiently. Among different discretization or approximation schemes, the commonly-used numeric approaches, such as finite difference and finite element formulations, are computationally expensive and hide the physics of the model. Black box techniques such as look up tables and neural networks are fast but offer no access to model parameters. Neither of these methods are, therefore, suitable to reduce distributed-parameter models for model-based design and control purposes.

Symbolic reduction methods, such as weighted residual schemes and variational principles³⁶, can generate reduced models which both expose the model parameters and are computationally efficient. If combined with symbolic simplification algorithms of computer algebra packages, such as Maple™, symbolic reduction methods can result in very efficient models. Further reduction of the so-obtained symbolic models is also possible by using advanced model order reduction schemes, such as the proper orthogonal decomposition.

Method of Weighted Residuals

The method of weighted residuals (MWR) is a general method of symbolically reducing time-dependent PDEs to ODEs³⁶ which encompasses several schemes, such as subdomain, collocation, Galerkin, and least squares methods. It is based on expanding the unknown solution as the finite summation of a set of known trial spatial functions multiplied by unknown time-varying coefficients. There are three important steps in the application of MWR: choice of trial functions, choice of a criterion (weighting functions), and calculation of weighted residuals. First, the approximate solution is substituted into the PDE to form a residual. Then, using a (complete) set of known weighting functions, the weighted integrals of the residual are set to zero to derive a set of ODEs from which the unknown coefficients can be computed.

The Galerkin method is one of the best known approaches where the weighting functions are chosen to be the same as the trial functions. The method forces the residual to be zero by making it orthogonal to each member of a complete set of functions. The method, however, is not suitable for nonlinear PDEs where the integrals of the weighted residual cannot be calculated analytically and may result in a very complex system of ODEs if a numerical integration has to be used. This is also true for other MWR schemes with other choices

of the weighting functions in which the analytic integration of the weighted residual is not feasible.

One exception is the collocation method in which the weighting functions are chosen to be the displaced Dirac delta functions. This choice of weighting functions reduces the integration over the domain to the evaluation at a point inside the domain. Thus, the method forces the residual to be zero at some specified collocation points and, since no spatial integration is required, it drastically reduces the drudgery of setting up the ODEs. It has proved to be suitable for nonlinear PDEs and when applicable, is highly recommended. It is worthwhile to note that the method can be as accurate as the Galerkin approach (and other MWR schemes) provided a high-order approximation is used. These higher order approximations are easily achievable by using the collocation method.

Orthogonal Collocation Method

In collocation methods, the low-order approximation results depend on the choice of collocation points. There are choices of collocation points that make the calculations more reliable and accurate. The orthogonal collocation method (OCM)^{36,37} uses a set of n orthogonal polynomials, up to order $(n - 1)$, as trial functions and the roots of the $(n + 1)$ th orthogonal polynomial (of order n) as collocation points. Thus the choice of collocation points is no longer arbitrary. The residual function is, therefore, forced to contain the $(n + 1)$ th orthogonal polynomial as a factor, because its zeros are set to match the roots to the $(n + 1)$ th polynomial. Due to orthogonality relations, the OCM has an accuracy that is comparable to that of the Galerkin method³⁷.

Noting that the OCM approximate solution only depends on the collocation points and not on the form of trial polynomials, two adjustments on trial polynomials are suggested and used in this work to expedite the reduction procedure. First, Lagrange polynomials of order $(n - 1)$, based on n nodal points, are used as trial functions to ensure that the unknown coefficients have the same physical meaning and order of magnitude (they would represent the solution at the nodal points). This helps in smoothing the behavior of the final ODEs. Second, the n nodal points of the Lagrange polynomials are set to coincide with the n collocation points. As shown in the following, this significantly simplifies the form of the final ODEs.

For illustration of how the suggested (modified) OCM can effectively reduce PDEs to a set of ODEs, consider a general nonlinear 1D PDE of the form:

$$\phi(y(x, t), \dot{y}(x, t), y'(x, t), x, t) = 0, \quad (43)$$

where ϕ is a general nonlinear function (boundary conditions are neglected for simplicity of description), x and t are the spatial coordinate and time, $y(x, t)$ is the unknown solution, and $\dot{y}(x, t)$ and $y'(x, t)$ are time and spatial derivatives of $y(x, t)$. The approximate solution is written as:

$$\bar{y}(x, t) = \sum_{i=1}^n Y_i(t) L_i(x), \quad (44)$$

where $Y_i(t) = Y_i$ are unknown coefficients and $L_i(x)$ are the Lagrange trial polynomials with nodal points \hat{x}_j :

$$L_i(x) = \prod_{j=1, j \neq i}^n \frac{x - \hat{x}_j}{\hat{x}_i - \hat{x}_j}. \quad (45)$$

Note that:

$$L_i(\hat{x}_j) = \delta_{ij} = \begin{cases} 1 & i = j \\ 0 & i \neq j \end{cases}, \quad (46)$$

where δ_{ij} is the Kronecker delta.

Substitution from equation (44) into equation (43) results in the residual function:

$$R(Y_i, \dot{Y}_i, x, t) = \phi\left(\sum_{i=1}^n Y_i L_i(x), \sum_{i=1}^n \dot{Y}_i L_i(x), \sum_{i=1}^n Y_i L_i'(x), x, t\right), \quad (47)$$

where $L_i'(x)$ is the spatial derivative of $L_i(x)$ with respect to x . The final ODEs are obtained by forming weighted residuals (the residual function evaluated at the collocation points \bar{x}_j) and setting them equal to zero:

$$W_j(Y_i, \dot{Y}_i, t) = R(Y_i, \dot{Y}_i, x, t) \Big|_{x=\bar{x}_j} = \phi\left(\sum_{i=1}^n Y_i L_i(\bar{x}_j), \sum_{i=1}^n \dot{Y}_i L_i(\bar{x}_j), \sum_{i=1}^n Y_i L_i'(\bar{x}_j), \bar{x}_j, t\right) = 0, \quad j = 1, \dots, n. \quad (48)$$

The n ODEs in equation (48) are the reduced form of the PDE given in equation (43).

Now, by recalling equation (46), for the case where the nodal points of the trial Lagrange polynomials are the same as the collocation points ($\hat{x}_j = \bar{x}_j$), the set of ODEs in equation (48) is reduced to:

$$W_j(Y_i, \dot{Y}_i, t) = \phi(Y_j, \dot{Y}_j, \sum_{i=1}^n Y_i L_i'(\hat{x}_j), \hat{x}_j, t) = 0, \quad j = 1, \dots, n, \quad (49)$$

which, for the case where ϕ is linear with respect to the \dot{y} , can be solved to obtain:

$$\dot{Y}_j = \phi'(Y_j, \sum_{i=1}^n Y_i L_i'(\hat{x}_j), \hat{x}_j, t), \quad j = 1, \dots, n. \quad (50)$$

A comparison between the ODEs given by equation (49) or (50) and those in equation (48) indicates that the modified OCM results in a set of ODEs which are decoupled to a great extent and, therefore, are significantly less expensive to solve. This modified OCM will be used to reduce the governing PDEs of the developed DPF model into a system of computationally-efficient ODEs as shown in the following section.

Numerical Results

In this section the accuracy and computational efficiency of the developed DPF model will be illustrated through some numerical examples. The examples consider a single ceramic wall-flow DPF, without the rest of the diesel after-treatment components, subjected to transient engine flows without cycle-by-cycle variations.

The model parameters for these examples (mainly corresponding to typical cordierite EX-80 100/17 and EX-80 200/12 filters^{9;10;13;38}) are given in Table 1. The examples are designed to describe the capabilities of the model in representing the nonlinear pressure drop, pressure-induced compressibility effects, and transient flow dynamics associated with a wall-flow DPF.

The modified OCM, suggested in the previous section, is implemented as a ninth-order approximation ($n = 9$) in Maple™ and is used to convert the 7 PDEs of the derived DPF model into a set of 63 ODEs. These ODEs are then numerically integrated in MapleSim™ by employing the “Implicit Euler” procedure, which is a fixed time-step solver in MapleSim™. To demonstrate the computational efficiency of the model, the required time for simulating each transient (unsteady) example (averaged over 5 runs on a desktop PC equipped with an Intel® Core™ i7-4790 @ 3.90 GHz CPU and 16 GB of RAM, running the 64-bit Windows 10) is measured and reported. The constant time-step is set to be 0.01 s for all the examples. One should be careful that, for the cases when the DPF model is fed with (high-frequency) engine cycle-by-cycle data, this time-step is not sufficiently small to capture the high-frequency time dependencies nor is it small enough to guarantee the convergence of the numerical time integrator. Accuracy and efficiency of the developed model in these cases will not be considered in this paper and will be left to a future work.

Table 1. Summary of the DPF model parameters (typical cordierite EX-80 100/17 and EX-80 200/12 filters)

Parameter	Value for	
	EX-80 100/17	EX-80 200/12
N	3006	6013
L	0.305 m	
D	2.11 mm	1.49 mm
σ_1, σ_2	1	
$C_{f,1}, C_{f,2}$	56.94	
Nu_1, Nu_2	3.61	
w_s	0.43 mm	0.31 mm
ε_s	48 %	
d_s	12 μm	
α'_s	150	
β'_s	1.75	
ρ_s	1290 kg/m^3	
k_s	2.093 $\text{W}/(\text{m} \cdot \text{K})$	
$C_{C_p,ss,i}$	$1.071 \times 10^{+3} \text{ J}/(\text{kg} \cdot \text{K})$	
$C_{C_p,ss,ii}$	$1.561 \times 10^{-1} \text{ J}/(\text{kg} \cdot \text{K}^2)$	
$C_{C_p,ss,iii}$	$-3.436 \times 10^{+7} \text{ J} \cdot \text{K}/\text{kg}$	
$w_{d,\text{ref}}$	3.5 μm	
$w_{d,\text{cr}}$	3.5 μm	
ε_d	72.5 %	
$d_{d,\text{min}}$	0.076 μm	
$d_{d,\text{max}}$	0.228 μm	
α'_d	150	
β'_d	1.75	
ρ_d	550 kg/m^3	
k_d	0.837 $\text{W}/(\text{m} \cdot \text{K})$	
S_d	$5.5 \times 10^{+7}/\text{m}$	
$C_{C_p,sd,i}$	$1.728 \times 10^{+3} \text{ J}/(\text{kg} \cdot \text{K})$	
$C_{C_p,sd,ii}$	$9.667 \times 10^{-2} \text{ J}/(\text{kg} \cdot \text{K}^2)$	
$C_{C_p,sd,iii}$	$-1.774 \times 10^{+8} \text{ J} \cdot \text{K}/\text{kg}$	
R_u	8.314 $\text{J}/(\text{mol} \cdot \text{K})$	
M_e	0.029 kg/mol	
R_e	286.7 $\text{J}/(\text{kg} \cdot \text{K})$	
$C_{p,e}$	1172 $\text{J}/(\text{kg} \cdot \text{K})$	
$C_{v,e}$	885.3 $\text{J}/(\text{kg} \cdot \text{K})$	
C_μ	$1.364 \times 10^{-6} \text{ kg}/(\text{m} \cdot \text{s} \cdot \text{K}^{1/2})$	
C_k	$3.586 \times 10^{+2} \text{ J}/(\text{kg} \cdot \text{K})$	
\mathcal{K}	596 $\text{m}/(\text{s} \cdot \text{K})$	
E	$1.5 \times 10^{+5} \text{ J}/\text{mol}$	
H_{CO}	$3.934 \times 10^{+5} \text{ J}/\text{mol}$	
H_{CO_2}	$0.984 \times 10^{+5} \text{ J}/\text{mol}$	
γ	0.6	
η_{min}	90 %	
η_{max}	100 %	
X_{in}	32×10^{-6}	
Y_{in}	0.154	
p_a	101.325 kPa	
T_a	300 K	

Example 1: Steady-State Flow in the Channels

As the first example, the DPF model is simulated under the steady-state conditions used by Konstandopoulos *et al.*¹⁶, *i.e.* inlet mass flow and temperature of 0.18 kg/s and 673 K (or inlet velocity and density of 24.8 m/s and 0.54 kg/m³).

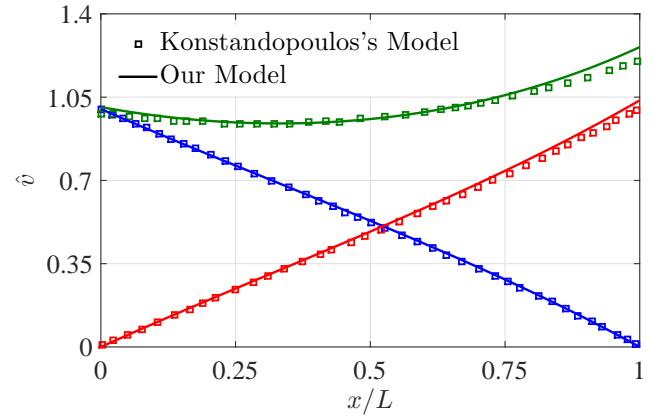


Figure 4. Dimensionless inlet (blue), outlet (red), and in-wall (green) velocities for a steady-state flow in a clean EX-80 100/17 DPF; our model prediction versus Konstandopoulos's 1D model data¹⁶.

The model parameters are those in Table 1 corresponding to the EX-80 100/17 filter (first column values) except that $\varepsilon_s = 43\%$.

The dimensionless inlet, outlet, and in-wall velocities are shown in Figure 4 and reasonably match those reported by Konstandopoulos *et al.*¹⁶ which are obtained using a 1D theoretical model and a 3D CFD model. These dimensionless velocities, *i.e.* inlet \hat{v}_1 , outlet \hat{v}_2 , and in-wall \hat{v}_0 , are defined as:

$$\hat{v}_1 = \frac{v_1}{v_{e,\text{in}}}, \quad \hat{v}_2 = \frac{v_2}{v_{e,\text{in}}}, \quad \hat{v}_0 = \frac{v_0}{v_{e,\text{in}}} \frac{4L}{D_1}. \quad (51)$$

Example 2: Transient Filter Loading and Nonlinear Pressure Drop

The second example is aimed at illustrating the nonlinear pressure drop of a wall-flow DPF during transient loading. The example is based on the experimental data reported by Suresh *et al.*³⁸ and Zhang *et al.*¹³ where a cordierite EX-80 200/12 filter is subject to inlet mass flow and temperature of 0.13 kg/s and 608 K. The model parameters are those in Table 1 corresponding to the EX-80 200/12 filter (second column values).

The predicted and measured³⁸ pressure drops across the filter during the 4-hour loading (filtration) process are depicted in Figure 5. No systematic parameter identification was performed to obtain the appropriate model parameters (only some minimal parameter tuning was done); however, Figure 5 illustrates the strong capability of the model to represent the nonlinear pressure drop behavior of DPFs.

It is also worthwhile to note that it only takes about 155 s to run this 4 h (14 400 s) simulation of a loading wall-flow DPF.

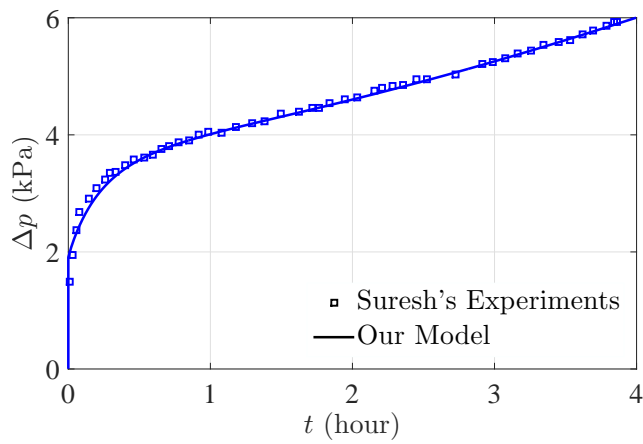


Figure 5. Nonlinear pressure drop variation during the loading of an EX-80 200/12 DPF; our model prediction versus experimental data reported by Suresh *et al.*³⁸.

Example 3: Transient Complete Regeneration

The third example describes a simple complete regeneration of a wall-flow DPF which was considered by Bissett *et al.*⁹. It is based on exposing a loaded wall-flow DPF, with a deposit layer of $11.17\ \mu\text{m}$ thickness, to an inlet flow of hot exhaust gas with mass flow rate and temperature of $0.038\ \text{kg/s}$ and $950\ \text{K}$. The model parameters are those in Table 1 corresponding to the EX-80 100/17 filter (first column values) except that $L = 0.254\ \text{mm}$.

The variations of the total pressure drop across the DPF and the maximum temperature inside the DPF substrate during the regeneration are shown in Figures 6 and 7. Again, considering the minimal parameter adjustments that were performed, the figures demonstrate a good agreement between the 1D model developed in this paper and the 1D model of Bissett *et al.*⁹.

The main observable difference is that our model predicts a faster regeneration process which starts sooner and, therefore, calculates a higher maximum temperature inside the DPF. This is even more evident in Figures 8 and 9 which show three snapshots of the wall temperature profile and the flux of wall mass flow rate (*i.e.* $\rho_0 v_0$) profile along the DPF length. Note that our model's snapshots at 22.4 s, 27.5 s and 51.5 s are equivalent to Bissett's model's snapshots at 26.5 s, 31.8 s and 63.6 s (those snapshots taken at the same time have significant differences).

Another point in Figures 8 and 9 is the fact that whereas the modified OCM with ninth-order approximating polynomials are enough for representing the smooth wall temperature variations inside the regenerating DPF, the stiffer wall-flow flux seems to require a higher-order approximation. It is interesting that, as expected, the approximate profiles in Figure 9 try to represent the actual

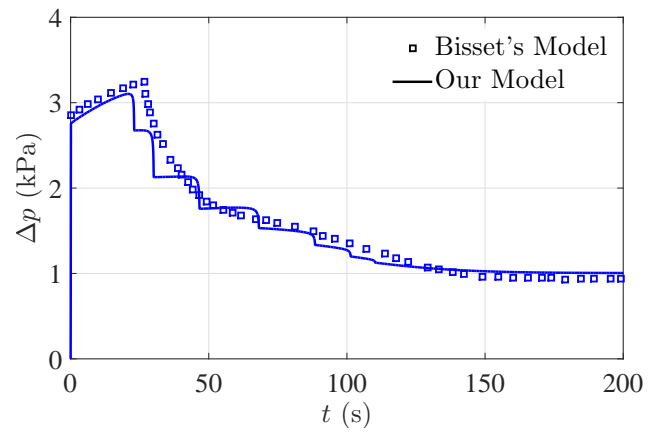


Figure 6. Nonlinear pressure drop variation during the regeneration of an EX-80 100/17 DPF; our model prediction versus Bissett's 1D model data⁹.

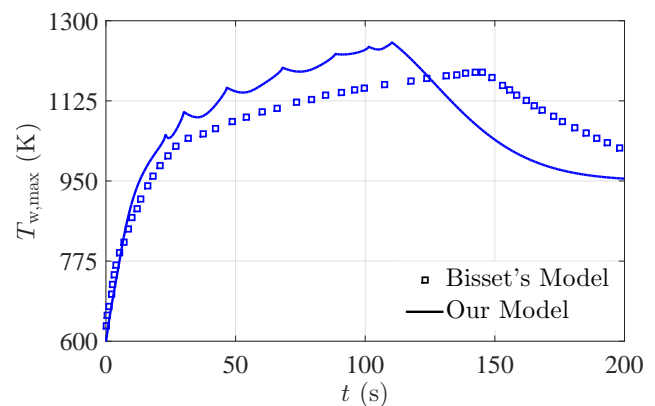


Figure 7. Maximum wall temperature variation during the regeneration of an EX-80 100/17 DPF; our model prediction versus Bissett's 1D model data⁹.

profiles on average and fluctuate about the actual profiles at different times.

Finally, it is noteworthy that this 200 s simulation of a regenerating wall-flow DPF takes only 2.2 s to be completed.

Conclusions

The physics-based DPF model developed in this study and its reduction by using the modified OCM have proved to result in a reduced DPF model which is both accurate and computationally efficient. The reduced model can be solved about 100 times faster than real time (with a fixed-step solver with 0.01 s time steps) and is capable of taking into account the compressibility and transient nature of the flow, the inertial terms of the pressure drop across the wall, and the nonlinear pressure drop behavior of the filter during the transient loading.

In contrast to most previous studies, *e.g.* Bissett *et al.*⁹, the work is not based on assuming a very thin deposit layer

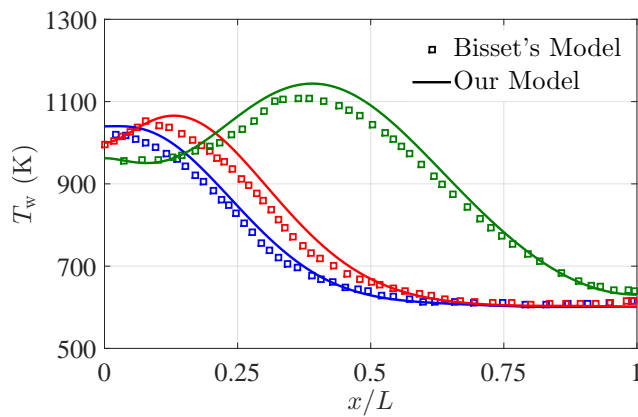


Figure 8. Snapshots of wall temperature during the regeneration of an EX-80 100/17 DPF; our model prediction at $t = 22.4$ s (blue), $t = 27.5$ s (red), and $t = 51.5$ s (green) versus Bisset's 1D model data⁹ at $t = 26.5$ s (blue), $t = 31.8$ s (red), and $t = 63.6$ s (green).

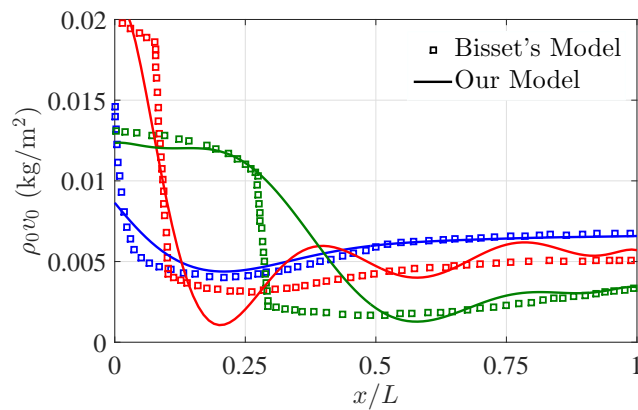


Figure 9. Snapshots of flux of wall mass flow rate during the regeneration of an EX-80 100/17 DPF; our model prediction at $t = 22.4$ s (blue), $t = 27.5$ s (red), and $t = 51.5$ s (green) versus Bisset's 1D model data⁹ at $t = 26.5$ s (blue), $t = 31.8$ s (red), and $t = 63.6$ s (green).

and filter substrate and takes into account the variations of the wall-flow velocity across the wall due to the trapezoidal shape of the wall cross section.

It is important to note that the inclusion of transient terms of the flow dynamics resulted in a reduced model governed by a system of only ODEs and not a system of differential-algebraic equations (DAEs). This is of great advantage because DAEs are computationally more expensive to solve than ODEs. In addition, most model order reduction schemes, such as the proper orthogonal decomposition method, can only be applied to models which are governed by pure ODEs. Finally, ODEs are required for most model-based control development.

The presented model is modular and each of its submodels (modules) can be updated if necessary. For example, the soot

oxidation submodel can be updated to represent the catalyzed regeneration of a catalytic DPF.

To close, it should be noted that the comparison between the accuracy of the full transient model presented in this paper with that of a quasi-steady model will be the subject of a future work. It would be of interest to see how the retained transient terms in mass, momentum, and energy equations may help to obtain more accurate results, in particular for cases when engine cycle-by-cycle flow, temperature, pressure, and emission data (with high-frequency time variations) are used to feed the DPF model.

Acknowledgements

This work was supported by the Natural Sciences and Engineering Research Council of Canada (NSERC), Toyota, and Maplesoft Inc.

References

1. Dinesen J, Nissen S and Christensen H. Electrochemical diesel particulate filter. Technical Report 980547, SAE Technical Paper, 1998. DOI:10.4271/980547.
2. Bissett E and Shadman F. Thermal regeneration of diesel-particulate monolithic filters. *AIChE Journal* 1985; 31(5): 753–758. DOI:10.1002/aic.690310508.
3. Filter Sensing Technologies, Inc. DPF Knowledge Base Technical Articles. URL: <http://www.fstcorporation.com/fst-dpf-knowledge-base.html>, 2015. URL <http://www.fstcorporation.com/fst-dpf-knowledge-base.html>. [Online; accessed 18-February-2015].
4. Adler J. Ceramic diesel particulate filters. *International Journal of Applied Ceramic Technology* 2005; 2(6): 429–439. DOI:10.1111/j.1744-7402.2005.02044.x.
5. Kladopoulou E, Yang S, Johnson J et al. A study describing the performance of diesel particulate filters during loading and regeneration—a lumped parameter model for control applications. Technical Report 2003-01-0842, SAE Technical Paper, 2003. DOI:10.4271/2003-01-0842.
6. Haralampous O, Kandylas I, Koltsakis G et al. Diesel particulate filter pressure drop part 1: Modelling and experimental validation. *International Journal of Engine Research* 2004; 5(2): 149–162. DOI:10.1243/146808704773564550.
7. Tang W, Wahiduzzaman S and Leonard A. A lumped/1-D combined approach for modeling wall-flow diesel particulate filters — applicable to integrated engine/aftertreatment simulations. Technical Report 2007-01-3971, SAE Technical Paper, 2007. DOI:10.4271/2007-01-3971.

8. Bissett E. Thermal regeneration of particle filters with large conduction. *Mathematical Modelling* 1985; 6(1): 1–18. DOI: 10.1016/0270-0255(85)90018-1.
9. Bissett E. Mathematical model of the thermal regeneration of a wall-flow monolith diesel particulate filter. *Chemical Engineering Science* 1984; 39(7): 1233–1244. DOI:10.1016/0009-2509(84)85084-8.
10. Koltsakis G and Stamatelos A. Modeling thermal regeneration of wall-flow diesel particulate traps. *AIChE Journal* 1996; 42(6): 1662–1672. DOI:10.1002/aic.690420618.
11. Koltsakis G and Stamatelos A. Modeling catalytic regeneration of wall-flow particulate filters. *Industrial & Engineering Chemistry Research* 1996; 35(1): 2–13. DOI:10.1021/ie950293i.
12. Koltsakis G and Stamatelos A. Modes of catalytic regeneration in diesel particulate filters. *Industrial & engineering chemistry research* 1997; 36(10): 4155–4165. DOI:10.1021/ie970095m.
13. Zhang Z, Yang S and Johnson J. Modeling and numerical simulation of diesel particulate trap performance during loading and regeneration. Technical Report 2002-01-1019, SAE Technical Paper, 2002. DOI:10.4271/2002-01-1019.
14. Opris C and Johnson J. A 2-D computational model describing the flow and filtration characteristics of a ceramic diesel particulate trap. Technical Report 980545, SAE Technical Paper, 1998. DOI:10.4271/980545.
15. Konstandopoulos A and Johnson J. Wall-flow diesel particulate filters — their pressure drop and collection efficiency. Technical Report 890405, SAE Technical Paper, 1989. DOI: 10.4271/890405.
16. Konstandopoulos A, Skaperdas E, Warren J et al. Optimized filter design and selection criteria for continuously regenerating diesel particulate traps. Technical Report 1999-01-0468, SAE Technical Paper, 1999. DOI:10.4271/1999-01-0468.
17. Konstandopoulos A, Kostoglou M, Skaperdas E et al. Fundamental studies of diesel particulate filters: transient loading, regeneration and aging. Technical Report 2000-01-1016, SAE Technical Paper, 2000. DOI:10.4271/2000-01-1016.
18. Masoudi M, Heibel A and Then P. Predicting pressure drop of wall-flow diesel particulate filters — theory and experiment. Technical Report 2000-01-0184, SAE Technical Paper, 2000. DOI:10.4271/2000-01-0184.
19. Konstandopoulos A, Skaperdas E and Masoudi M. Inertial contributions to the pressure drop of diesel particulate filters. Technical Report 2001-01-0909, SAE Technical Paper, 2001. DOI:10.4271/2001-01-0909.
20. Masoudi M, Konstandopoulos A, Nikitidis M et al. Validation of a model and development of a simulator for predicting the pressure drop of diesel particulate filters. Technical Report 2001-01-0911, SAE Technical Paper, 2001. DOI:10.4271/2001-01-0911.
21. Konstandopoulos A, Skaperdas E and Masoudi M. Microstructural properties of soot deposits in diesel particulate traps. Technical Report 2002-01-1015, SAE Technical Paper, 2002. DOI:10.4271/2002-01-1015.
22. Piscaglia F and Ferrari G. Development of an offline simulation tool to test the on-board diagnostic software for diesel after-treatment systems. Technical report, SAE Technical Paper, 2007. DOI:10.4271/2007-01-1133.
23. Swift S, Glover K and Collings N. Safe operation and control of diesel particulate filters using level set methods. In Blondel V, Boyd S and Kimura H (eds.) *Recent Advances in Learning and Control, Lecture Notes in Control and Information Sciences*, volume 371. London, England: Springer. ISBN 978-1-84800-154-1, 2008. pp. 233–247. DOI:10.1007/978-1-84800-155-8_17.
24. Torregrosa A, Serrano J, Arnau F et al. A fluid dynamic model for unsteady compressible flow in wall-flow diesel particulate filters. *Energy* 2011; 36(1): 671–684. DOI:10.1016/j.energy.2010.09.047.
25. Serrano J, Climent H, Piqueras P et al. Filtration modelling in wall-flow particulate filters of low soot penetration thickness. *Energy* 2016; 112: 883–898. DOI:10.1016/j.energy.2016.06.121.
26. Ferrari G, Piscaglia F and Onorati A. 1D modeling of the hydrodynamics and of the regeneration mechanism in continuous regenerating traps. Technical report, SAE Technical Paper, 2006. DOI:10.4271/2006-01-3011.
27. Cunningham P and Meckl P. 1-D dynamic diesel particulate filter model for unsteady pulsating flow. Technical report, SAE Technical Paper, 2007. DOI:10.4271/2007-01-1140.
28. Piscaglia F and Ferrari G. A novel 1D approach for the simulation of unsteady reacting flows in diesel exhaust after-treatment systems. *Energy* 2009; 34(12): 2051–2062. DOI: 10.1016/j.energy.2008.08.022.
29. NGK Insulators, Ltd. Sic-dpf and cordierite-dpf. URL: http://www.ngk.co.jp/english/news/2001/image/2001_05_14_a_01.jpg, 2001. URL http://www.ngk.co.jp/english/news/2001/image/2001_05_14_a_01.jpg. [Online; accessed 17-March-2016].
30. Pritchard P. *Fox and McDonald's introduction to fluid mechanics*. 8th ed. Hoboken, NJ, USA: John Wiley & Sons, 2011. ISBN 9780470547557. URL <http://books.google.ca/books?id=1hhYLwEACAAJ>.
31. Kreith F, Manglik R and Bohn M. *Principles of heat transfer*. 7th ed. Stamford, CT, USA: Cengage Learning, 2010. ISBN 9780495667704. URL <http://books.google>.

ca/books?id=1hVSQBnr74C.

32. Bissett E, Kostoglou M and Konstandopoulos A. Frictional and heat transfer characteristics of flow in square porous tubes of wall-flow monoliths. *Chemical Engineering Science* 2012; 84: 255–265. DOI:10.1016/j.ces.2012.08.012.
33. Macdonald I, El-Sayed M, Mow K et al. Flow through porous media — the Ergun equation revisited. *Industrial & Engineering Chemistry Fundamentals* 1979; 18(3): 199–208. DOI:10.1021/i160071a001.
34. Opris C and Johnson J. A 2-D computational model describing the heat transfer, reaction kinetics and regeneration characteristics of a ceramic diesel particulate trap. Technical Report 980546, SAE Technical Paper, 1998. DOI:10.4271/980546.
35. Johnson J, Bagley S, Gratz L et al. A review of diesel particulate control technology and emissions effects - 1992 horning memorial award lecture. Technical Report 940233, SAE technical paper, 1994. DOI:10.4271/940233.
36. Finlayson B. *The method of weighted residuals and variational principles, Classics in applied mathematics*, volume 73. Philadelphia, PA, USA: Society for Industrial and Applied Mathematics, 2013. ISBN 9781611973242. DOI:10.1137/1.9781611973242.
37. Villadsen J and Stewart W. Solution of boundary-value problems by orthogonal collocation. *Chemical Engineering Science* 1967; 22(11): 1483–1501. DOI:10.1016/0009-2509(67)80074-5.
38. Suresh A, Khan A and Johnson J. An experimental and modeling study of cordierite traps-pressure drop and permeability of clean and particulate loaded traps. Technical Report 2000-01-0476, SAE Technical Paper, 2000. DOI: 10.4271/2000-01-0476.

Appendix: Derivation of Filter Wall Equations

This appendix provides more details on derivation of the previously-mentioned equations governing the flow (see equations (4) and (8)), accumulation and oxidation of the particles (see equations (11) and (29)), pressure drop (see equations (9), (12), and (13)), and oxygen depletion (see equation (27)) over the wall of wall-flow DPFs.

It is firstly useful to recall equations (1), (2), and (3), describing the geometry of the wall system in a wall-flow

DPF, and summarize them in (see Figure 3 or 10):

$$\begin{aligned} D_1 &= D_2 - 2w_d, \\ P_1 &= 4D_1, \quad A_1 = D_1^2, \\ P_2 &= 4D_2, \quad A_2 = D_2^2, \\ A_s &= 4\left(D_2 + \frac{w_s}{2}\right)w_s, \\ A_d &= 4\left(D_2 - w_d\right)w_d. \end{aligned} \quad (52)$$

In-Wall Mass Flow Rate

The in-wall mass flow rate per unit length of the channel \dot{m}_0 is one of the key terms when modeling wall-flow DPFs. It can be expressed as the product of the in-wall (cross-sectional) perimeter and the wall-flow density and velocity. Assuming a quasi-steady wall-flow that has no component in the axial direction (*i.e.* along x -axis in Figure 3) one can conclude that, despite the variations of the in-wall perimeter and wall-flow density and velocity in the lateral direction (*i.e.* y -axis in Figure 3 or 10), the in-wall mass flow rate \dot{m}_0 as the product of these parameters remains constant in the wall (y), *i.e.*:

$$\dot{m}_0 = \rho P v = \text{constant}, \quad (53)$$

where ρ and v are the wall-flow density and velocity (which may vary in the lateral direction along the y -axis) and P is the local perimeter inside the wall system. Note that based on the ideal gas law:

$$\rho = \frac{p}{R_e T_0}, \quad (54)$$

where p and T_0 are the wall-flow local pressure and average temperature. Moreover, based on the schematics shown in Figure 10 and by recalling equation (52), one can write:

$$P = 4D, \quad D = \begin{cases} D_1 + 2y & 0 \leq y \leq w_d + \frac{w_s}{2} \\ D_2 + 2\left(w_s + w_d - y\right) & w_d + \frac{w_s}{2} < y \leq w_d + w_s \end{cases} \quad (55)$$

The in-wall mass flow rate \dot{m}_0 can also be represented in terms of the in-wall perimeter and the wall-flow density and velocity at a reference point (or surface) in the lateral direction. Selecting this point to be right on the surface of the filter substrate in the inlet channel (*i.e.* at $y = w_d$ in Figure 10), the in-wall mass flow rate will be:

$$\begin{aligned} \dot{m}_0 &= \rho_0 P_2 v_0, \\ \rho_0 &= \frac{p_0'}{R_e T_0} \approx \frac{p_0}{R_e T_0}, \end{aligned} \quad (56)$$

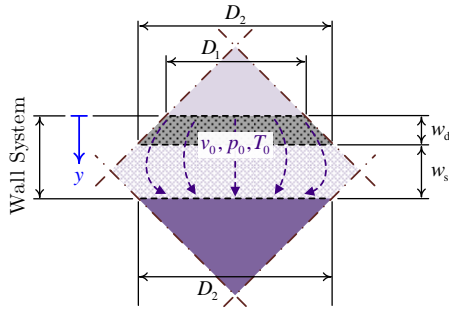


Figure 10. Schematic geometry of the wall system corresponding to a quarter inlet/outlet channel set, and in-wall flow pattern.

where ρ_0 , v_0 , and p_0' are wall-flow density, velocity, and pressure at $y = w_d$ and p_0 is the wall-flow average pressure. In equation (56), the average wall-flow pressure p_0 , taken as the mean value of the pressures in the inlet and outlet channels, is assumed to differ only slightly from the wall-flow pressure at $y = w_d$, i.e. p_0' . This is a reasonable assumption considering that, for a clean filter, the pressure drop across the wall is very small, usually about 1% of the pressures inside the DPF channels, and, therefore, the average pressure p_0 differs by only 0.5% from the pressure on the lateral surface of the inlet channel at $y = w_d$. Moreover, for a loaded filter, due to the nonlinear pressure drop behavior of the deposit layer, usually a main portion of the wall pressure drop takes place over the very thin layer of the deposit that is initially formed on the surface of the filter substrate^{9;14;20}. Therefore, the average wall-flow pressure p_0 usually occurs inside the deposit layer but very close to the lateral surface of the inlet channel at $y = w_d$.

On-Wall Particle Accumulation and Oxidation

During the filtration, the rate of the mass of particles accumulated on the lateral surface of the inlet channel (per unit length of the channel), i.e. $\frac{\partial m_{d,f}}{\partial t}$, can be calculated from the DPF filtration efficiency η , the mass fraction of the particulate matter in the exhaust gas X_1 , and the in-wall mass flow \dot{m}_0 :

$$\frac{\partial m_{d,f}}{\partial t} = \eta X_1 \dot{m}_0. \quad (57)$$

During the regeneration, note that the molar rate of oxygen depletion inside the wall can be calculated as the product of the in-wall exhaust gas molar flow rate $\frac{\dot{m}_0}{M_e}$ and the variation of the oxygen molar concentration across the wall $\Delta Y = Y_1 - Y_2$. Thus, by using the molecular weight of carbon M_C , the rate of the mass of particles oxidized on the lateral surface of the inlet channel (per unit length of the channel),

i.e. $\frac{\partial m_{d,r}}{\partial t}$, can be obtained as:

$$\frac{\partial m_{d,r}}{\partial t} = -M_C \frac{\dot{m}_0}{M_e} \Delta Y \frac{2}{1+\gamma}, \quad (58)$$

where recall that, based on the reaction given by equation (25) or (26), each mode of oxygen depleted in the wall will oxidize $\frac{2}{1+\gamma}$ mode of carbon particles.

Combining equations (57) and (58), the overall mass rate of the particles accumulated and oxidized (during filtration and regeneration) on the lateral surface of the inlet channel (per unit length of the channel), i.e. $\frac{\partial m_d}{\partial t}$, can be written as:

$$\begin{aligned} \frac{\partial m_d}{\partial t} &= \frac{\partial m_{d,f}}{\partial t} + \frac{\partial m_{d,r}}{\partial t} \\ &= \dot{m}_0 \left(\eta X_1 - \frac{M_C}{M_e} \Delta Y \frac{2}{1+\gamma} \right). \end{aligned} \quad (59)$$

Assuming that the deposit layer density ρ_d remains constant during the filtration and regeneration, the rate of change of the deposit layer cross-sectional area, i.e. $\frac{\partial A_d}{\partial t}$, can be calculated from $\frac{\partial m_d}{\partial t}$ as:

$$\frac{\partial A_d}{\partial t} = \frac{1}{\rho_d} \left(\frac{\partial m_d}{\partial t} \right). \quad (60)$$

Separately, the last relation in equation (52) can be used and differentiated with respect to time to find:

$$\frac{\partial A_d}{\partial t} = 4 \left(D_2 - 2w_d \right) \frac{\partial w_d}{\partial t} = P_1 \frac{\partial w_d}{\partial t}, \quad (61)$$

where equation (52) is recalled (also see Figure 10). Now, one can substitute from equation (61) into equation (60) to obtain the overall rate of change of the deposit layer thickness during the filtration and regeneration, i.e. $\frac{\partial w_d}{\partial t}$, as:

$$\begin{aligned} \frac{\partial w_d}{\partial t} &= \frac{1}{P_1} \left(\frac{\partial A_d}{\partial t} \right) = \frac{1}{\rho_d P_1} \left(\frac{\partial m_d}{\partial t} \right) \\ &= \frac{\dot{m}_0}{\rho_d P_1} \left(\eta X_1 - \frac{M_C}{M_e} \Delta Y \frac{2}{1+\gamma} \right) \\ &= \frac{\rho_0 P_2 v_0}{\rho_d P_1} \left(\eta X_1 - \frac{M_C}{M_e} \Delta Y \frac{2}{1+\gamma} \right), \end{aligned} \quad (62)$$

where substitutions from equations (59) and (56) are used to derive the final form.

In equation (62), note that the rate of change of the deposit layer thickness during the filtration and regeneration, i.e. $\frac{\partial w_{d,f}}{\partial t}$ and $\frac{\partial w_{d,r}}{\partial t}$ respectively, are individually identified to be:

$$\begin{aligned} \frac{\partial w_{d,f}}{\partial t} &= \frac{\rho_0 P_2 v_0}{\rho_d P_1} \left(\eta X_1 \right), \\ \frac{\partial w_{d,r}}{\partial t} &= \frac{\rho_0 P_2 v_0}{\rho_d P_1} \left(-\frac{M_C}{M_e} \Delta Y \frac{2}{1+\gamma} \right). \end{aligned} \quad (63)$$

In-Wall Pressure Drop

As noted previously, the quasi-empirical correlation suggested by Ahmed and Sunada combined with the modified Ergun equation^{19,33} can be used to predict the pressure drop across the wall system in a wall-flow DPF.

The general form of the Ahmed and Sunada equation, correlating the velocity vector inside a porous medium to the gradient of the pressure, is:

$$-\vec{\nabla}p = \alpha \mu \vec{v} + \beta \rho \|\vec{v}\| \vec{v}, \quad (64)$$

where $\vec{\nabla}p$ is the pressure gradient vector, μ and ρ are the viscosity and density of the fluid, \vec{v} is the flow velocity vector inside the porous medium, and α and β are the porous medium parameters to be empirically established. A well-known model for determination of the coefficients α and β in equation (64) in terms of the porous medium parameters is the modified Ergun equation which suggest that:

$$\alpha = \alpha' \frac{(1-\varepsilon)^2}{\varepsilon^3 d^2}, \quad \beta = \beta' \frac{(1-\varepsilon)}{\varepsilon^3 d}, \quad (65)$$

where ε is the porosity of the medium, d is the an appropriate characteristic length of the medium (e.g. mean pore size), and coefficients α' and β' are nondimensional constants to be determined experimentally. A good assumption for these constants is $\alpha' = 150$ and $\beta' = 1.75$ as appeared in the original Ergun equation³³.

Considering Figure 10 and taking into account only the (1D) wall-flow and pressure drop along the y -axis, perpendicular to the wall system including the porous deposit layer and the porous filter substrate, equation (64) can be employed to write:

$$-\frac{dp}{dy} = \begin{cases} \alpha_d \mu_0 v + \beta_d \rho v^2 & 0 \leq y \leq w_d \\ \alpha_s \mu_0 v + \beta_s \rho v^2 & w_d < y \leq w_d + w_s \end{cases}, \quad (66)$$

where:

$$\begin{aligned} \alpha_s &= \alpha'_s \frac{(1-\varepsilon_s)^2}{\varepsilon_s^3 d_s^2}, & \beta_s &= \beta'_s \frac{(1-\varepsilon_s)}{\varepsilon_s^3 d_s}, \\ \alpha_d &= \alpha'_d \frac{(1-\varepsilon_d)^2}{\varepsilon_d^3 d_d^2}, & \beta_d &= \beta'_d \frac{(1-\varepsilon_d)}{\varepsilon_d^3 d_d}. \end{aligned} \quad (67)$$

By assuming that all the parameters in equations (66) and (67), except the wall-flow density ρ and velocity v , keep a constant average value over the wall thickness (during both filtration and regeneration), one can integrate equation (66) to obtain an expression for the total pressure drop across the wall system.

For the deposit layer (i.e. $0 \leq y \leq w_d$), one can use equation (53) and rewrite equation (66) as:

$$-\frac{dp}{dy} = \alpha_d \mu_0 \left(\frac{\dot{m}_0}{\rho P} \right) + \beta_d \rho \left(\frac{\dot{m}_0}{\rho P} \right)^2, \quad (68)$$

which, by using equation (54), can be rearranged to:

$$-\frac{1}{Re T_0} p dp = \alpha_d \mu_0 \left(\frac{\dot{m}_0}{P} \right) dy + \beta_d \left(\frac{\dot{m}_0}{P} \right)^2 dy. \quad (69)$$

By substitution from equation (55), one can integrate equation (69) over the deposit layer thickness (from $y = 0$ to $y = w_d$) and obtain:

$$\begin{aligned} \frac{1}{2 Re T_0} (p_1^2 - p_0'^2) &= \alpha_d \mu_0 \left(\frac{\dot{m}_0}{4} \right) \frac{1}{2} \ln \left(\frac{D_2}{D_1} \right) \\ &+ \beta_d \left(\frac{\dot{m}_0}{4} \right)^2 \frac{w_d}{D_2 D_1}, \end{aligned} \quad (70)$$

where equation (52) is used and recall that p_0' is the wall-flow pressure at $y = w_d$. Analogously, for the substrate layer (i.e. $w_d < y \leq w_d + w_s$), one can obtain:

$$\begin{aligned} \frac{1}{2 Re T_0} (p_0'^2 - p_2^2) &= \alpha_s \mu_0 \left(\frac{\dot{m}_0}{4} \right) \ln \left(\frac{D_2 + w_s}{D_2} \right) \\ &+ \beta_s \left(\frac{\dot{m}_0}{4} \right)^2 \frac{w_s}{D_2 (D_2 + w_s)}. \end{aligned} \quad (71)$$

Now, equations (70) and (71) can be added together to write:

$$\begin{aligned} \frac{1}{2 Re T_0} (p_1^2 - p_2^2) &= \frac{p_1 + p_2}{2 Re T_0} (p_1 - p_2) = \\ &\left(\alpha_d \frac{1}{2} \ln \left(\frac{D_2}{D_1} \right) + \alpha_s \ln \left(\frac{D_2 + w_s}{D_2} \right) \right) \mu_0 \left(\frac{\dot{m}_0}{4} \right) \\ &+ \left(\beta_d \frac{w_d}{D_2 D_1} + \beta_s \frac{w_s}{D_2 (D_2 + w_s)} \right) \left(\frac{\dot{m}_0}{4} \right)^2. \end{aligned} \quad (72)$$

By noting that $p_0 = \frac{p_1 + p_2}{2}$ and recalling equations (56) and (52), one can simplify equation (72) to obtain an expression for the pressure drop across the wall system (including both deposit and substrate layers):

$$\begin{aligned} \Delta p &= p_1 - p_2 \\ &= \left(\alpha_d \frac{1}{2} \ln \left(\frac{D_2}{D_1} \right) + \alpha_s \ln \left(\frac{D_2 + w_s}{D_2} \right) \right) \mu_0 D_2 v_0 \\ &+ \left(\beta_d \frac{w_d}{D_2 D_1} + \beta_s \frac{w_s}{D_2 (D_2 + w_s)} \right) \rho_0 D_2^2 v_0^2 \\ &= \left(\alpha_d \frac{D_2}{2} \ln \left(\frac{D_2}{D_1} \right) + \alpha_s D_2 \ln \left(\frac{D_2 + w_s}{D_2} \right) \right) \mu_0 v_0 \\ &+ \left(\beta_d \frac{D_2 w_d}{D_1} + \beta_s \frac{D_2 w_s}{D_2 + w_s} \right) \rho_0 v_0^2. \end{aligned} \quad (73)$$

In-Wall Oxygen Depletion

Consider the schematics shown in Figure 10 and in particular focus on the section through the deposit layer rather than the sections through the filter substrate or the channels. Based on the assumptions noted previously and the reaction given by equation (25) or (26), the oxygen balance equation inside the porous deposit layer (where the whole oxidation occurs) can be written as^{2,10}:

$$\frac{d}{dy} \left(Y \frac{\dot{m}_0}{M_e} \right) = -P S_d K_d Y \frac{\rho}{M_e} \left(\frac{1+\gamma}{2} \right), \quad (74)$$

where Y is the oxygen molar concentration at each point y inside the deposit layer ($0 \leq y \leq w_d$). It is useful to mention that $Y \frac{\dot{m}_0}{M_e}$ is the molar flow rate of oxygen at each point inside the deposit layer and $Y \frac{\rho}{M_e}$ is the molar density of oxygen at that point.

Noting that $\frac{\dot{m}_0}{M_e}$ remains constant through the deposit layer, the relation in equation (74) can be rewritten as:

$$\frac{\dot{m}_0}{M_e} \left(\frac{dY}{dy} \right) = -P S_d K_d Y \frac{\rho}{M_e} \left(\frac{1+\gamma}{2} \right), \quad (75)$$

which by substitution from equation (53) can be simplified to:

$$\frac{dY}{dy} = -S_d K_d Y \left(\frac{1+\gamma}{2} \right) \frac{1}{v}, \quad (76)$$

or, after the separation of variables:

$$\frac{dY}{Y} = -S_d K_d \left(\frac{1+\gamma}{2} \right) \frac{dy}{v}. \quad (77)$$

By neglecting the variations of the wall-flow density in the deposit layer and assuming the wall-flow density ρ to be equal to the average wall-flow density ρ_0 (implying that $Pv = P_2 v_0$ or $Dv = D_2 v_0$ in the deposit layer), equation (77) can be integrated over the deposit layer thickness to derive an expression for the variation of the oxygen molar concentration across the deposit layer ΔY_d :

$$\frac{\Delta Y_d}{Y_1} = 1 - \exp \left(-S_d K_d \left(\frac{1+\gamma}{2} \right) \frac{D_2 w_d - w_d^2}{D_2 v_0} \right), \quad (78)$$

where equation (52) is recalled. Because it is assumed that there is no reaction occurring inside the porous ceramic substrate layer, ΔY_d would be equal to the change in the oxygen molar concentration across the whole wall system (including the porous deposit layer and the filter porous ceramic substrate), *i.e.* ΔY , and one can write:

$$\Delta Y = Y_1 - Y_2 = \Delta Y_d. \quad (79)$$

Nomenclature

English Letters

A	Channel cross-sectional area
C	Heat capacity
D	Channel hydraulic diameter
E	Reaction activation energy
H	Reaction heat (enthalpy)
K	Reaction rate coefficient
L	Channel length
M	Molecular weight
N	Number of inlet channels
P	Channel perimeter
R	Gas constant
S	Specific area
T	Temperature
X	Mass fraction (of particles)
Y	Mole fraction (of oxygen)
c	Convection heat transfer coefficient
d	Pore size (pore diameter)
f	Friction coefficient
h	Enthalpy
k	Conduction heat transfer coefficient (thermal conductivity)
m	Mass
p	Pressure
q	Heat added to the system per unit length
s	Entropy
t	Time
u	Internal energy
v	Velocity
w	Thickness
x	Axial coordinate
y	First lateral coordinate

z	Second lateral coordinate	$\square_{\text{CO}_{1+\gamma}}$	Incomplete carbon oxidation product ($\text{CO}_{1+\gamma}$)
Calligraphic Letters		\square_{cr}	Critical value
\mathcal{C}	General coefficient	\square_{d}	Porous deposit layer
\mathcal{K}	Collisions frequency factor	\square_{e}	Exhaust gases
Greek Letters		\square_{f}	Filtration
Δ	Difference (delta)	\square_{g}	Generated
α	First pressure drop coefficient	\square_{i}	Inlet/outlet channel (flow); $i = 1$ for inlet channel and $i = 2$ for outlet channel
α'	Coefficient in the first pressure drop coefficient relation	\square_{in}	Incoming (inlet) flow conditions
β	Second pressure drop coefficient	\square_{min}	Minimum
β'	Coefficient in the second pressure drop coefficient relation	\square_{max}	Maximum
γ	Completeness index for soot (carbon) oxidation	\square_{O}	Oxygen
ε	Porosity	\square_{o}	Outer
η	Filtration efficiency	\square_{out}	Outgoing (outlet) flow conditions
κ	Kinetic energy coefficient	\square_{p}	At constant pressure
μ	Dynamic viscosity	\square_{r}	Regeneration
π	Number π	\square_{ref}	Reference value
ρ	Density	\square_{s}	Porous substrate
σ	Linear momentum coefficient	\square_{sd}	Solid deposit
ϕ, ϕ'	General (nonlinear) function	\square_{ss}	Solid substrate
Multi-Letter Symbols		\square_{sys}	System
Re	Reynolds number	\square_{u}	Universal
Nu	Nusselt number	\square_{v}	At constant volume
Subscripts		\square_{w}	Wall (<i>i.e.</i> deposit layer plus substrate layer)
\square_0	Wall-flow		
\square_1	Inlet channel (flow)		
\square_2	Outlet channel (flow)		
\square_{a}	Ambient		
\square_{C}	Carbon		
\square_{c}	Convection		
\square_{CO}	Carbon monoxide (CO)		
\square_{CO_2}	Carbon dioxide (CO ₂)		